Optical Society of America. Cheng Ma, Bo Dong, Jianmin Gong, and Anbo Wang, "Decoding the spectra of low-finesse extrinsic optical fiber Fabry-Perot interferometers," Opt. Express 19, 23727-23742 (2011). doi: 10.1364/OE.19.023727

Decoding the spectra of low-finesse extrinsic optical fiber Fabry-Perot interferometers

Cheng Ma,* Bo Dong, Jianmin Gong and Anbo Wang

Center for Photonics Technology, Bradley department of Electrical and Computer Engineering, Virginia Polytechnic Institute and State University, Blacksburg, VA 24061-0111, USA

**cma1@vt.edu*

Abstract: A theoretical model is developed to address the fringe visibility and additional phase in the interference spectra of low-finesse extrinsic optical fiber excited Fabry-Pérot interferometers. The model described in the paper applies to both single-mode and multimode fiber excitations; according to the theory, the fringe visibility and additional phase term are primarily determined by the working wavelength and angular power density distribution outputting from the excitation fiber, rather than based on spatial and temporal degree of coherence. Under certain approximations, the output interference intensity and the spatial power density distribution projected onto the fiber axis form a Fourier-transform pair, which potentially provides a tool for spatial density distribution analysis of fiber output. With excellent agreement with experiments, the theory presented in this paper leads to design guidelines for Fabry-Pérot interferometric sensors and insightful physical understanding of such devices.

OCIS codes: (060.2370) Fiber optics sensors; (060.2310) Fiber optics; (120.2230) Fabry-Pérot; (120.3180) Interferometry; (120.2650) Fringe analysis; (050.1940) Diffraction.

References and links

1. C. E. Lee and H. F. Taylor, "Fiber-optic Fabry-Perot temperature sensor using a low-coherence light source," Lightwave Technology Journalism **9**, 129–134 (1991).
2. Y. Zhu, Z. Huang, F. Shen, and A. Wang, "Sapphire-fiber-based white-light interferometric sensor for high-temperature measurements," Opt. Lett. **30**(7), 711–713 (2005).
3. C. Belleville and G. Duplain, "White-light interferometric multimode fiber-optic strain sensor," Opt. Lett. **18**(1), 78–80 (1993).
4. A. Wang, H. Xiao, J. Wang, Z. Wang, W. Zhao, and R. G. May, "Self-Calibrated Interferometric-Intensity-Based Optical Fiber Sensors," J. Lightwave Technol. **19**(10), 1495–1501 (2001).
5. Y. Kim and D. P. Neikirk, "Micromachined Fabry-Perot cavity pressure transducer," IEEE Photon. Technol. Lett. **7**(12), 1471–1473 (1995).
6. N. Fürstenau, M. Schmidt, H. Horack, W. Goetze, and W. Schmidt, "Extrinsic Fabry-Perot interferometer vibration and acoustic sensor systems for airport ground traffic monitoring," IEEE Proc. Optoelectron. **144**(3), 134–144 (1997).
7. B. Qi, G. R. Pickrell, J. Xu, P. Zhang, Y. Duan, W. Peng, Z. Huang, W. Huo, H. Xiao, R. G. May, and A. Wang, "Novel data processing techniques for dispersive white light interferometer," Opt. Eng. **42**(11), 3165–3171 (2003).
8. M. Han, Y. Zhang, F. Shen, G. R. Pickrell, and A. Wang, "Signal-processing algorithm for white-light optical fiber extrinsic Fabry-Perot interferometric sensors," Opt. Lett. **29**(15), 1736–1738 (2004).
9. F. Shen and A. Wang, "Frequency-estimation-based signal-processing algorithm for white-light optical fiber Fabry-Perot interferometers," Appl. Opt. **44**(25), 5206–5214 (2005).
10. S. Tretter, "Estimating the frequency of a noisy sinusoid by linear regression (Corresp.)," IEEE Trans. Info. Theory **31**(6), 832–835 (1985).
11. C. Ma and A. Wang, "Multimode excitation-induced phase shifts in intrinsic Fabry-Perot interferometric fiber sensor spectra," Appl. Opt. **49**(25), 4836–4845 (2010).
12. C. Ma, E. Lally, and A. Wang, "Toward Eliminating Signal Demodulation Jumps in Optical Fiber Intrinsic Fabry-Perot Interferometric Sensors," to be published in J. Lightwave Technol. (2011).
13. V. Arya, M. de Vries, K. A. Murphy, A. Wang, and R. O. Claus, "Exact Analysis of the Extrinsic Fabry-Perot Interferometric Optical Fiber Sensor Using Kirchhoff's Diffraction Formalism," Opt. Fiber Technol. **1**(4), 380–384 (1995).
14. F. Pérennès, P. C. Beard, and T. N. Mills, "Analysis of a low-finesse Fabry-Perot sensing interferometer illuminated by a multimode optical fiber," Appl. Opt. **38**(34), 7026–7034 (1999).

#151186 - $15.00 USD Received 15 Jul 2011; accepted 29 Aug 2011; published 8 Nov 2011

15. M. Han and A. Wang, "Exact analysis of low-finesse multimode fiber extrinsic Fabry-Perot interferometers," Appl. Opt. **43**(24), 4659–4666 (2004).
16. M. Han and A. Wang, "Mode power distribution effect in white-light multimode fiber extrinsic Fabry-Perot interferometric sensor systems," Opt. Lett. **31**(9), 1202–1204 (2006).
17. M. Born and E. Wolf, *Principles of optics: electromagnetic theory of proagation, interference and diffraction of light,* 7 ed. (Cambrige University Press, 2003).
18. A. Yariv, *Optical electronics in modern communications,* 5th ed. (Oxford University Press, Inc., 1997).
19. E. D. Becker and T. C. Farrar, "Fourier Transform Spectroscopy: New methods dramatically improve the sensitivity of infrared and nuclear magnetic resonance spectroscopy," Science **178**(4059), 361–368 (1972).
20. M. Artiglia, G. Coppa, P. Di Vita, M. Potenza, and A. Sharma, "Mode field diameter measurements in single-mode optical fibers," Lightwave Technology Journalism **7**, 1139–1152 (1989).
21. Y. Kokubun and K. Iga, "Mode analysis of graded-index optical fibers using a scalar wave equation including gradient-index terms and direct numerical integration," J. Opt. Soc. Am. **70**(4), 388–394 (1980).
22. G. Keiser, *Optical Fiber Communications* (McGraw-Hill, Boston,Mass., 2000).

1. Introduction

The spectrum of fiber optic low-finesse extrinsic Fabry-Pérot (FP) interferometers (EFPIs) is studied in this research. Such fiber coupled interferometers have been demonstrated as highly sensitive and robust sensors for measurement of temperature [1, 2], strain [3], pressure [4, 5] and acoustic wave [6]. White-light interferometry [7], in which the interferometer is illuminated either by a broadband optical source or a wavelength-tunable laser and its reflected spectrum is analyzed, has shown promising advantages over other interrogation counterparts in terms of demodulation accuracy, absolute measurement and immunity to optical power instability. In order to make accurate and reliable measurements, the sensor spectrum needs to be characterized carefully, some advanced signal processing algorithms have been developed to this end [7–9]. While it is well understood that the demodulation error scales with noise power in the spectrum [10], the demand for high fringe visibility becomes crucial, especially if a multimode fiber (MMF) is used for excitation. During the past few years, it has been reported in several publications [8, 11, 12] that the additional phase in the spectrum also plays an important role in signal processing, which may potentially lead to abrupt jumps in the demodulated sensor cavity length. As such, in-depth theoretical modeling for both single-mode fiber (SMF) and MMF based EFPIs have been investigated in the past two decades [8, 13–15], aiming to find the dependence of sensor output spectrum on sensor geometry and optical property.

Arya *et al.* [13] addressed the fringe visibility of SMF-EFPI by considering diffraction in the interferometer cavity, the similar approach was extended to study the beam propagation (diffraction) and re-coupling induced additional phase term by Han *et al.* [8]. While SMF-EFPI manifests well-defined electromagnetic (EM) field profile in the cavity, MMF-EFPI does not: because MMF can have very diverse mode excitation conditions, each guided mode has its individual mode profile yet the phase differences among the excited modes are extremely complex, this poses considerable difficulties in modeling the MMF-EFPI. Pérennès *et al.* [14] developed a simple geometrical-optics approach, their theory led to an analytical solution for the fringe visibility, but was not sufficiently accurate for many real applications. Han *et al.* [15, 16] treated the problem with a more rigorous EM field approach using optical fiber mode theory, and both the fringe visibility and additional phase issues have been addressed. All the above theories contributed to our understanding of the EFPI fiber sensor behavior; however, several key issues still remained unsolved.

The models based on rigorous EM field treatments, although promising in computing good numerical solutions, encounter difficulties at bridging the physical model with real-world applications, for example, mode excitation in MMF can be very complex, and may vary upon multiple environmental factors; all these factors can couple together to make the problem extremely complicated. In addition, several basic questions have yet been satisfactorily answered. In experiments, it is found that the fringe visibilities of MMF-EFPIs typically fade much faster as the cavity lengths increase than SMF-EFPIs do. How does this phenomenon relate to the temporal and spatial degree of coherence of the output light from the excitation fiber? In intrinsic Fabry-Pérot interferometric (IFPI) sensors, the cavity-length-dependent additional phase can ultimately lead to demodulation discontinuities [12]. Will this

#151186 - $15.00 USD Received 15 Jul 2011; accepted 29 Aug 2011; published 8 Nov 2011

additional phase also behave similarly for the EFPI sensors? In principle, any fiber can experience a smooth transition from single mode-few mode-multimode operation without clear boundaries. Is there a unified theory applicable to all these working conditions? The theory described in this paper aims to solve these problems.

2. Theory

2.1 Fundamental concepts

The subject is optical fiber low-finesse EFPIs. By "low-finesse", it refers to weak reflections created by the air-dielectric interfaces. For the two types of dielectric materials typically encountered in EFPIs—silica and sapphire, the power reflectivities are approximately 4% and 7% respectively, sufficiently small to neglect multiple reflections inside the FP cavity. The word "extrinsic" refers to free-space propagation of the optical beam inside the cavity, as in contrast to "intrinsic", in which case the propagation of the beam is assumed to be guided.

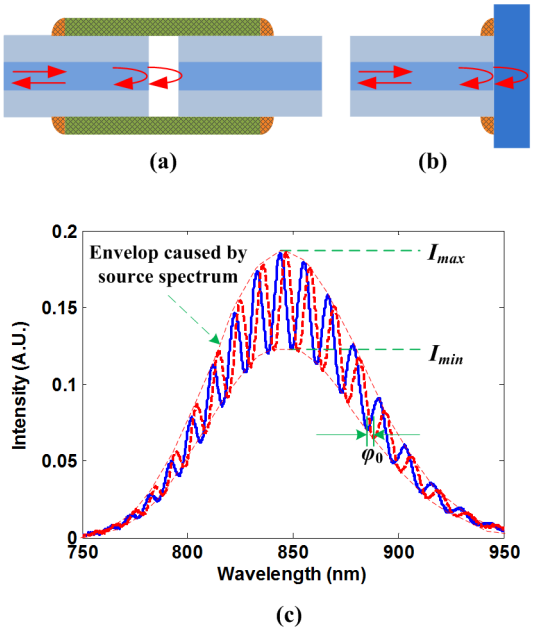

Fig. 1. EFPI sensor schematics and spectrum. (a) EFPI sensor with air-gap cavity. (b) EFPI sensor with wafer cavity. (c) a typical sensor spectrum.

The free-space propagation of the light can either be in air or in dielectric. For the former, the two reflections are formed by two polished optical fiber ends, and the two fibers are aligned inside a capillary tube, as shown in Fig. 1(a). For the case of propagation in dielectrics, the excitation fiber is placed in adjacent to a (glass or sapphire) wafer, and the two reflections are generated on both sides of the wafer, as shown in Fig. 1(b). In both geometries, the two weak reflections possess certain phase relationship determined by the physical cavity length (e.g., optical path difference (OPD), defined as OPD = $2nL$, n is the refractive index of the dielectric (n = 1 for air) and L is the physical cavity length) and the two beams are coupled back into the lead-in fiber and interfere. The interference spectrum is then obtained to calculate the OPD encoded. A typical EFPI interference spectrum is illustrated in Fig. 1(c). The total phase of the sinusoid in the spectrum can be expressed as:

$$\Phi = k \cdot \mathrm{OPD} + \varphi_0 \tag{1}$$

In the above equation, k is the wavenumber defined as $k=2\pi/\lambda$, λ is the wavelength, and φ_0 is the additional phase we discussed in Section 1, which could cause the spectrum to shift (without a change in the density of the fringes). In Fig. 1(c), the red dashed curve and the blue

#151186 - $15.00 USD Received 15 Jul 2011; accepted 29 Aug 2011; published 8 Nov 2011

solid one have a phase difference of π/2. By identifying the maximum and minimum intensities in the fringe, the fringe visibility (FV) is calculated as:

$$\mathrm{FV} = \frac{I_{\max} - I_{\min}}{I_{\max} + I_{\min}} \tag{2}$$

2.2 The EFPI spectrum

Before proceeding to the theory, we will briefly introduce the physical model representing the subject matter. We will focus on EFPI structures with air-gap cavities (as shown in Fig. 1(a)), and our conclusion can be easily extended to a wafer-based cavity. For sensor geometry illustrated in Fig. 1(a), if the distance between the two reflective surfaces is sufficiently long, and the divergence angle of the optical beam is sufficiently large, light can reach the inner wall of the capillary tube and be partially reflected. In this regard the light propagation can no longer be treated as "free space", but rather partially guided, which tend to significantly complicate the analysis. In light of the above considerations, we will avoid such complications by applying the model illustrated in Fig. 2.

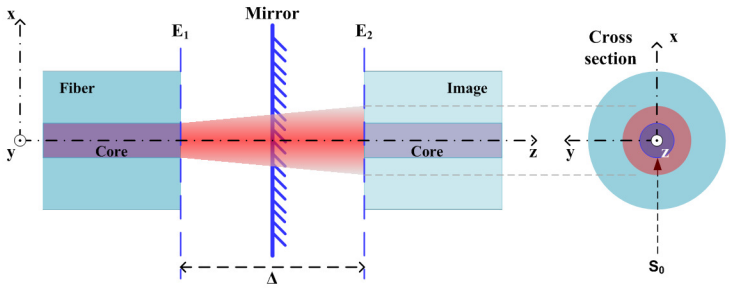

Fig. 2. Schematic of the optical fiber low-finesse EFPI

In the model, one of the two reflections is generated by the fiber- air interface and the other by an infinite mirror in the x-y plane with the same reflectivity; the two mirror surfaces are perpendicular to the fiber axis (*z* axis). In the FP cavity, light propagates in +z direction, after getting reflected by the mirror, it propagates in the –z direction for the same distance and is re-coupled back into the lead-in fiber. This whole process is physically equivalent to the case in which the reflected light keeps propagating in free space along +z direction for another cavity length, Δ/2, and couples into an image fiber whose axis is aligned with the lead-in fiber (this equivalence does not strictly hold in terms of the intensity and phase of the light, this will be addressed during the following mathematical deduction). The propagation distance inside the cavity is thus the OPD of the interferometer, and is denoted as Δ. We denote the electric field at the first fiber end plane with complex amplitude E_1 and that at the second plane (image fiber end-face) with E_2. In the following analysis, all fields are treated as scalar wave functions as in most diffraction problems. Such an approximation is adequate for the model considered [17] and from now on we neglect the influence of the light polarization. Because for the current study we only care about the relative intensity, in order to simplify the mathematical expressions we take out a constant ($1/2\eta$, η being the vacuum impedance) from the expressions for optical intensity. For the sake of simplicity without losing its generality, the mirror is assumed to have the same reflectivity as the fiber end-face, we also neglect the power loss due to the Fresnel reflection at the fiber end-face (as in Ref [15], we adopt this approximation for the clarity and simplicity of the mathematical expressions), thus the two interfering fields become rE_1 and rE_2, where r is the field reflectivity. For the same reason stated above, we take out the constant r and consider the interference between E_1 and E_2.

The detected power is the intensity on the fiber end-face integrated over the fiber core area S_0, and can be expressed as

#151186 - $15.00 USD Received 15 Jul 2011; accepted 29 Aug 2011; published 8 Nov 2011

$$P = \iint_{S_0} \left(E_1 + E_2\right)^* \left(E_1 + E_2\right) ds \tag{3}$$

The integration in Eq. (3) can be split into four terms,

$$\iint_{S_0} E_1 E_1^* ds = P_1 \tag{4.1}$$

$$\iint_{S_0} E_2 E_2^* ds = \nu P_1 \tag{4.2}$$

$$\iint_{S_0} E_1 E_2^* ds = \iint_{\infty} E_1 E_2^* ds \tag{4.3}$$

$$\iint_{S_0} E_2 E_1^* ds = \left(\iint_{S_0} E_1 E_2^* ds \right)^* \tag{4.4}$$

In the above expressions, P_1 denotes the reflected power by the fiber end-face, v is the power coupling coefficient into the mirror fiber. We substitute the integration region S_0 with infinity in Eq. (4.3) because E_1 is approximated as only present in the fiber core.

We define the plane of the fiber end-face to be $z = 0$, and the plane of the image fiber end-face to be $z = \Delta$, for the following derivation we confine our calculation to a monochromatic wave with wavevector k, and expand the field E_1 as the superposition of plane waves (2-D Fourier-transform)

$$E_1\left(x, y, 0\right) = \iint E\left(k_x, k_y\right) \cdot \exp\left[i\left(k_x x + k_y y\right)\right] dk_x dk_y \tag{5}$$

In the above expression, k_x and k_y are the x and y components of the wavevector. Explicit expression of the field at the $z = \Delta$ plane stems from the diffraction of E_1 to the $z > 0$ free space (considering propagation along the z axis) [18]

$$E_2\left(x, y, \Delta\right) = \iint E\left(k_x, k_y\right) \cdot \exp\left[i\left(k_x x + k_y y - k_z \Delta - \pi\right)\right] dk_x dk_y \tag{6}$$

where $k_z = \sqrt{k^2 - k_x^2 - k_y^2}$ is the z component of the wavevector and the phase delay π arises from the reflection from the second mirror. Inserting Eq. (5) and Eq. (6) into Eq. (4.3), we obtain

$$\begin{aligned} \iint_{\infty} E_1 E_2^* ds = \iint \iint \iint E\left(k_x, k_y\right) E^*\left(k_x', k_y'\right) \cdot \\ \exp\left\{i\left[\left(k_x - k_x'\right)x + \left(k_y - k_y'\right)y + k_z \Delta + \pi\right]\right\} dk_x dk_y dk_x' dk_y' dxdy \end{aligned} \tag{7}$$

Notice that the integrations over x and y are performed in the entire infinite plane, and the following equation should hold to simplify the integration in Eq. (7)

$$\int_{\infty} \exp\left[i\left(k_\mu - k_\mu'\right)\mu\right] d\mu = \delta\left(k_\mu - k_\mu'\right) \tag{8}$$

where $\mu = x$, y and $\delta(x)$ denotes the Dirac delta function. Inserting Eq. (8) into Eq. (7) gives

$$\iint_{\infty} E_1 E_2^* ds = \iint \left|E\left(k_x, k_y\right)\right|^2 \cdot \exp\left[i\left(k_z \Delta + \pi\right)\right] dk_x dk_y \tag{9}$$

Combining Eq. (9) and Eq. (4.4) results in

$$\iint_{S_0} \left(E_1 E_2^* + E_2 E_1^*\right) ds = -2 \iint_{\infty} \left|E\left(k_x, k_y\right)\right|^2 \cdot \cos\left(k_z \Delta\right) dk_x dk_y \tag{10}$$

#151186 - $15.00 USD Received 15 Jul 2011; accepted 29 Aug 2011; published 8 Nov 2011

The integration in Eq. (10) is in the *k*-space Cartesian coordinate. We then convert it to integration in the polar system and further integrate over k_φ to remove the azimuthal dependence on φ (φ denotes the angle between the polar vector and the x-axis) as long as mathematical separation of variables between k_r and k_φ holds (which is a reasonable assumption for most cases). Also bear in mind that the square of the absolute value of the E-field gives the intensity

$$\iint_{S_0}\left(E_1E_2^{*}+E_2E_1^{*}\right)ds=-2\int I\left(k_r\right)\cdot\cos\left(k_z\Delta\right)k_r dk_r \tag{11}$$

In the above equation, $I(k_r)$ can be interpreted as power density distribution projected onto the radial direction (i.e., spatial density distribution projected onto the x-y plane), by using the relationship $k_r^2+k_z^2=k^2$, the integration over k_r can be converted to integration over k_z; by combining Eq. (11) with Eqs. (4.1~4.2), the total received power can be expressed as:

$$P=\left(1+\nu\right)P_1-2\int_0^k I\left(k_z\right)\cdot\cos\left(k_z\Delta\right)k_z dk_z \tag{12}$$

In Eq. (12), $I(k_z)$ is the optical power density distribution along the fiber axis (z) in the FP cavity (not in the fiber). Equation (12) is the general expression for the received power. Before stepping forward to calculate the fringe visibility and additional phase in the interferogram, it is interesting to explore the physical message encoded in this equation.

If the optical beam inside the FP cavity has a sufficiently small divergence angle, such that $I(k_z)$ is distributed over a very narrow k_z range, Eq. (12) can be simplified as

$$P\left(\Delta\right)=C_0\int_0^{\infty} I\left(k_z\right)\left[1-\cos\left(k_z z\right)\right]dk_z \tag{13}$$

with C_0 being a constant. The second term on the right-hand-side of Eq. (13) shows the Fourier cosine transform relationship between the power density distribution of a monochromatic light projected onto the z axis and the OPD dependent output power from the low-finesse EFPI. It manifests the Fourier cosine transform relationship between the spectral density distribution and the output intensity from a Michelson interferometer, which is the basis for Fourier-transform spectroscopy [19]. Equation (13) can be regarded as a *k*-domain counterpart of the Wiener-Khintchine theorem.

Equation (12) can be written as

$$P\left(\Delta\right)=\left(1+\nu\right)P_1-2\int_0^k I\left(k_z\right)\cdot\cos\left(\left(k_z-k\right)\Delta+k\Delta\right)k_z dk_z \tag{14}$$

After expanding the cosine term in the above integration and some mathematical rearrangement, the spectrum obtained from the EFPI is expressed as

$$P\left(\Delta\right)=Q\left(\Delta\right)\left[1+\frac{\sqrt{C^2\left(\Delta\right)+S^2\left(\Delta\right)}}{Q\left(\Delta\right)}\cos\left(k\Delta+\theta\left(\Delta\right)+\pi\right)\right] \tag{15}$$

In the above equation

$$\theta\left(\Delta\right)=\tan^{-1}\left(-\frac{C\left(\Delta\right)}{S\left(\Delta\right)}\right)+\frac{\pi}{2} \tag{16}$$

is the additional phase term stems from the optical beam free space beam propagation, the fringe visibility of the spectrum $FV(\Delta)$ is expressed by

#151186 - $15.00 USD Received 15 Jul 2011; accepted 29 Aug 2011; published 8 Nov 2011

$$FV(\Delta) = \frac{\sqrt{C^2(\Delta) + S^2(\Delta)}}{Q(\Delta)} \tag{17}$$

in which

$$C(\Delta) = 2\int_0^k I(k_z) \cdot \cos\left(\left(k_z - k\right)\Delta\right) k_z dk_z \tag{18}$$

$$S(\Delta) = 2\int_0^k I(k_z) \cdot \sin\left(\left(k_z - k\right)\Delta\right) k_z dk_z \tag{19}$$

$$Q(\Delta) = (1+\nu) P_1 \tag{20}$$

It is interesting to compare the result in Eq. (15) with the calculated spectrum from a Michelson interferometer used as a Fourier-transform spectrometer in [17], where the source spectral distribution was treated by considering the fringe induced by each monochromatic spectral component and adding up the interference pattern generated by each component incoherently. Similarly, Eq. (12) inherently suggests the same physics for an optical source with certain spatial power density distribution (divergent from unidirectional): the overall interference spectrum is the incoherent superposition of the interference patterns generated by individual plane wave components with different propagation directions. Surprisingly, the fringe visibility shown in Eq. (17) depends neither on spatial nor on spectral coherence, as one may expect that the visibility would decrease as the degree of coherence drops. In other words, the conclusion drawn here is in contradiction to our common sense: intuitively, the fringe visibility should be larger for EFPIs illuminated by a highly coherent laser than for those excited by a incoherent broadband source; also the visibility should be larger for light with higher spatial coherence (such as a single mode fiber) than light which is nearly incoherent spatially (such as highly multimode fiber); however, in reality the fringe visibility is solely determined by the working wavelength and spatial power density distribution (projected onto z axis) as shown in Eq. (17). It is predicted possible that a SMF-EFPI illuminated by a highly coherent laser can have less fringe visibility than a MMF -EFPI illuminated with a halogen light bulb, as is experimentally demonstrated in Section 3.4.

2.3 Calculation of $I(k_z)$

The fringe visibility and additional phase are shown to be determined by the power density distribution projected onto z axis (Eqs. (15)-(19)). Notice that the "distribution projected onto z axis" subjects to a monochromatic light (with a fixed wavenumber k); light with a different wavelength may have a different z-distribution, thus the fringe visibility and additional phase are wavelength-dependent, as will be demonstrated in Section 3.2. In order to calculate the fringe visibility and additional phase according to Eq. (17) and Eq. (16) respectively, the $I(k_z)$ distribution needs to be determined in advance. Calculation of $I(k_z)$ employs different approaches for SMF-based and MMF-based EFPIs.

$I(k_z)$ calculation for SMF-based EFPIs

For a typical SMF, the field distribution on the fiber cross section can be well-approximated as a Gaussian [20]

$$E(x, y) = \exp\left[-\left(x^2 + y^2\right)\Big/ w_0^2\right] \tag{21}$$

where w_0 denotes the mode field radius of the fiber. The 2-D Fourier-transform of Eq. (21) can be readily obtained as

$$E\left(k_x, k_y\right) = \frac{w_0^2}{8\pi^2} \exp\left[-w_0^2\left(k_x^2 + k_y^2\right)\Big/ 4\right] \tag{22}$$

#151186 - $15.00 USD Received 15 Jul 2011; accepted 29 Aug 2011; published 8 Nov 2011

By inserting the relationship $k_z^2 = k^2 - \left(k_x^2 + k_y^2\right)$ into Eq. (22), we get the $I(k_z)$ distribution as

$$I\left(k_z\right) = I_0 \exp\left[-w_0^2\left(k^2 - k_z^2\right)/2\right] \tag{23}$$

where I_0 is a constant, k is the wavenumber, and k_z is in the range between 0 to k.

$I(k_z)$ calculation for MMF-based EFPI

For MMF-based EFPI, analytical expression for $I(k_z)$ is extremely difficult to obtain. With hundreds, even thousands of modes being excited, accurate calculation of the relative intensity and phase of each mode can be too complex to be practical. One can assume the absolute value of the general field profile to be approximated by a well-defined function (e.g., a Gaussian as in the SMF case), but calculating the Fourier-transform is also impractical due to the unknown phase profile across the fiber end-face. Fortunately, only the power density distribution (instead of the field distribution) is needed for the calculation of the fringe characteristic, and this power distribution can be directly calculated by measuring the output angular power distribution, as shown in Fig. 3.

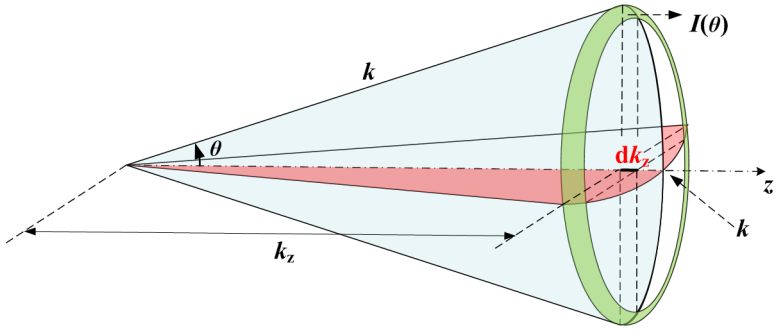

Fig. 3. Conversion schematic from angular power density distribution to the k_z density distribution. The total power distributed from k_z to $k_z + dk_z$ is equal to the power flux in the ring area (in green color) defined by divergence angle from θ to $\theta + d\theta$

As shown in Fig. 3, light with k_z component falling within the range between k_z to $k_z + dk_z$ has total power of

$$I\left(k_z\right)dk_z = 2\pi \cdot k \cdot I\left(\theta\right)dk_z \tag{24}$$

with $I(\theta)$ being the power density distribution with respect to divergence angle θ. Equation (24) directly leads to the following relationship between the power density distribution projected onto the z axis and along θ direction

$$I\left(k_z\right) = 2\pi k \cdot I\left(\theta\right) = 2\pi k \cdot I\left[\operatorname{acos}\left(k_z/k\right)\right] \tag{25}$$

Equation (25) demonstrates that the $I(k_z)$ distribution can be obtained by the knowledge of the angular distribution $I(\theta)$, as will be shown in Section 3.2; $I(\theta)$ can be determined by measuring the optical far field power distribution of the multimode fiber.

3. Results and discussion

3.1 SMF-EFPI: simulation and experimental results

Figure 4 shows the experimental setup to measure the fringe visibility curves for both SMF and MMF-EFPIs. The two reflections of the low-finesse Fabry-Pérot interferometer were formed by a polished distal end of the lead-in fiber and an optical-quality surface on a silica pentaprism. We chose the pentaprism to eliminate the back-reflection from the far-end, which might affect the measurement accuracy of the fringe visibility. Parallelism of the two surfaces forming the FP cavity was guaranteed by maximizing the fringe visibility at a given cavity

#151186 - $15.00 USD Received 15 Jul 2011; accepted 29 Aug 2011; published 8 Nov 2011

length; tuning of the mirror angles was achieved by two rotation stages in perpendicular planes, as shown in Fig. 4. Two types of fibers were used in the experiment: Corning SMF-28 standard single mode fiber and Nufern UHNA7 ultra-high NA single mode fiber. Light from a highly-coherent tunable laser (coherent length ≈30 cm, tuning range from 1520 nm to 1570 nm) was coupled into the lead-in fiber via a fiber circulator, and the reflected interference signal was sent to the spectrometer through the same circulator. The spectrometer used was the high precision Component Testing System (*Si-720,* Micron Optics, Inc.), spectral resolution rating of the instrument was below 5 pm. During the measurement, the cavity length of the FP interferometer was adjusted using a one-dimensional translation stage; fringe visibility at 1550 nm was calculated at each cavity length (OPD), the cavity length was calculated based on the interferogram with estimated accuracy well below 50nm [9].

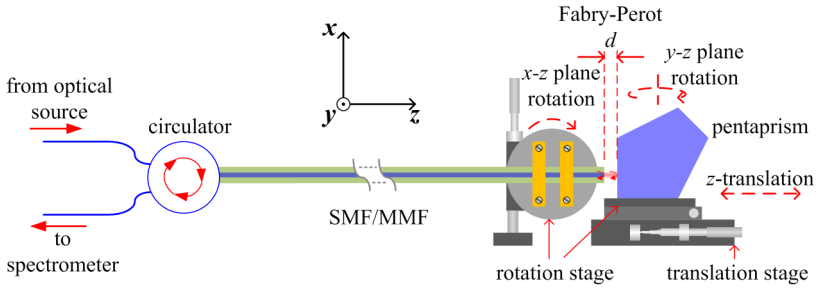

Fig. 4. Experimental setup for measurement of the fringe visibility curve. Parallelism of the two reflection surfaces are guaranteed by tuning the two rotation stages, and the cavity length can be finely tuned by a 1-D translation stage.

The visibility measurement results for both types of single mode fibers are plotted in Fig. 5; also plotted in the same figure are the simulation results. For the simulation we used Eq. (17) to calculate the visibility; prior to the visibility calculation, $I(k_z)$ was determined using Eq. (23). The value of the unknown parameter w_0 (fiber mode field radius) in Eq. (23) was adjusted during the simulation to acquire best agreement with experiment. The mode field radii calculated for SMF-28 and UHNA7 fibers were 4.9 and 1.7 μm, respectively; they agreed well with their corresponding specifications, which were 5.2+/–0.4 μm and 1.6 +/– 0.15 μm. In Fig. 5, circles and dots are experimental data; solid and dashed curve are simulation results. The sensitivity of the fringe visibility to the mode field diameter of the input fiber suggests potentially a novel method to characterize the mode field diameter of single mode fibers: by characterizing the visibility curve, w_0 can be calculated by fitting the experimental data using Eqs. (17) and (23).

#151186 - $15.00 USD Received 15 Jul 2011; accepted 29 Aug 2011; published 8 Nov 2011

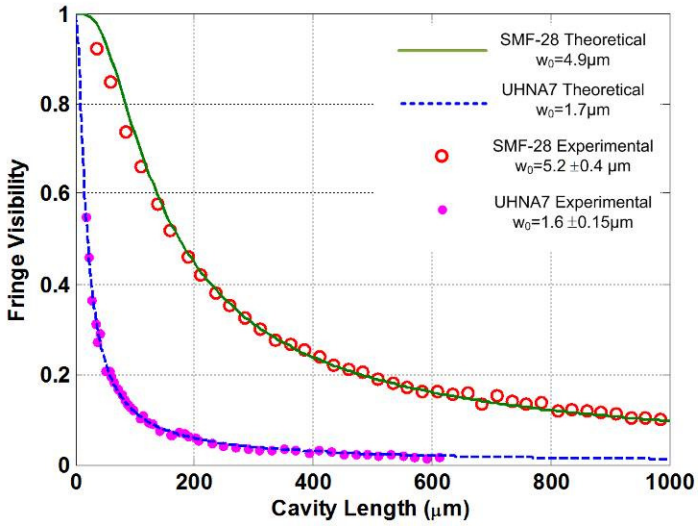

Fig. 5. Fringe visibility plotted as a function of FP cavity length. Solid and dashed curves represent simulation results, circles and dots are experimental data. The calculated mode field radii of the fibers are labeled and compared with the values in their specifications.

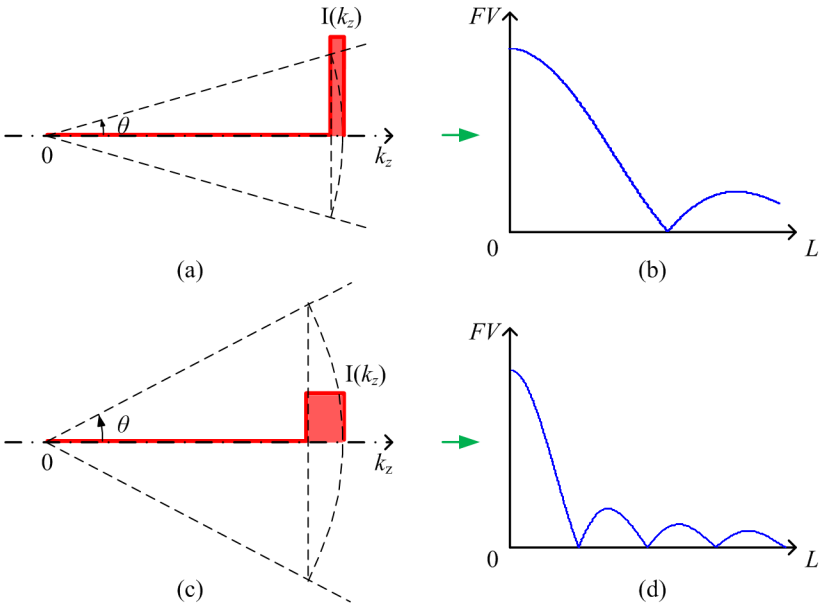

Fig. 6. Conceptual illustration of the relationship between output divergence angle and the visibility curve. (a) $I(k_z)$ distribution of a beam with less divergence angle. (b) Visibility curve corresponding to the distribution in (a). (c) $I(k_z)$ distribution of a beam with larger divergence angle. (d) Visibility curve corresponding to the distribution in (c). The figures show qualitatively that the visibility curve gets broader as $I(k_z)$ becomes sharper.

The fringe visibility of the UHNA7 fiber based EFPI drops much faster than the SMF-28 fiber based EFPI as the cavity length increases, which can be explained as follows. The high NA fiber has a smaller mode field diameter, in other words, the Gaussian profile used to approximate the field has a narrower width. With the waist of the output Gaussian beam coincides with the fiber distal end, the fiber mode field radius can be regarded as the Gaussian

#151186 - $15.00 USD Received 15 Jul 2011; accepted 29 Aug 2011; published 8 Nov 2011

beam waist size. The divergence angle of the Gaussian beam is inversely proportional to its beam waist size w_0 by [18]

$$\theta = \frac{\lambda}{\pi w_0} \tag{26}$$

According to Eq. (26), light divergence angle is much larger for the UHNA7 fiber than the SMF28 fiber due to its smaller waist size. A larger divergence angle leads to a broader $I(k_z)$ distribution, as shown in Fig. 3 and Eq. (25). As discussed in Section 2.2, the Fourier-transform pair formed by the interferometer output power and the $I(k_z)$ distribution implies a simple relationship: the broader the $I(k_z)$ distribution, the sharper the visibility curve (means the visibility drops faster with increasing OPD). This is analogous to the case of Fourier transform spectroscopy: for optical source with higher temporal coherence, its narrower spectral density distribution results in more slowly dropping visibility. Figure 6 conceptually illustrates the above conclusion.

The extra phase delay θ in Eq. (15) has also been studied using SMF-28 based EFPI. Theoretical and experimental data are provided in Fig. 7. To calculate the phase term, Eqs. (16), (18), (19), and (23) were employed. Notice the good agreement between the result shown in Fig. 7 with that reported in [8], in which the phase term was attributed to free space beam propagation and re-coupling back to the fiber. Equation (12) gives another physical interpretation of this extra phase shift. Plane waves (at a fixed wavelength) with different k_z components, when propagating inside the FP cavity, will experience different OPDs (thus different total phase delay) due to various divergence angles. The component normal to the reflection mirrors has no extra phase delay, but other components tend to manifest additional phase shifts depending on their injection angles; the overall effect is the superposition of all these extra phases as an effective phase term in the total fringe pattern. In plotting Fig. 7, when the cavity length is short, θ is difficult to be accurately measured from the fringe pattern due to signal processing limitations; whereas at longer cavity lengths, the fringe visibility is very low resulting in poor signal to noise ratio (SNR), which is responsible for the relatively large noises in the experimental data.

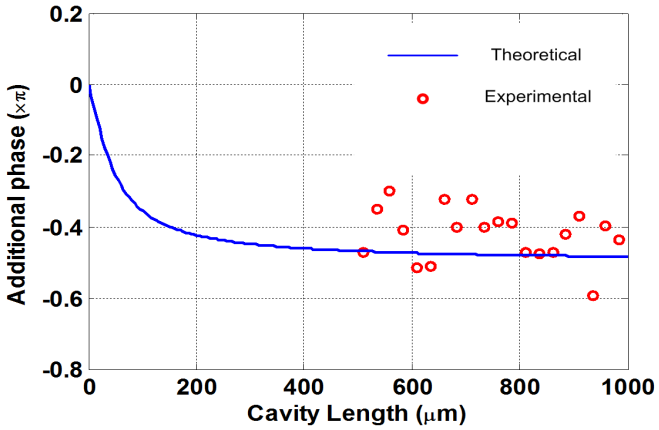

Fig. 7. Theoretical and experimental data showing the extra phase delay of an EFPI with SMF-28 as the lead-in fiber

3.2 MMF-EFPI: comparison with previous literatures

In this subsection, multimode fiber with 'uniform mode excitation' will be studied. Under this condition, all the modes in the multimode fiber will be excited with equal power which will generate a top-hat shaped output angular distribution [14]. In reality, this condition is unlikely to occur due to mode filtering and mixing effects during wave propagation in the fiber which tends to build up a steady 'equilibrium' mode distribution [21]. However, analysis of this

#151186 - $15.00 USD Received 15 Jul 2011; accepted 29 Aug 2011; published 8 Nov 2011

idealized case is important because: 1. it yields a simple analytical solution and 2. it sets a theoretical standard to characterize and compare the performances of different MMFs. Thus previous theoretical works paid considerable attention to analyze this situation [14, 15].

We will apply Eq. (25) with Eq. (17) to calculate the fringe visibility. At such excitation condition, $I(k_z)$ distribution can be expressed as

$$I(k_z)=\begin{cases}\text{constant}, & 0<\text{acos}(k_z/k)<\text{asin}(\text{NA})\\ 0, & \text{others}\end{cases} \tag{27}$$

When inserting Eq. (27) into Eqs. (17)-(20), the calculation can be dramatically simplified by assuming the beam to diverge gently (with small output angle), which helps to drop the k_z terms in the integrations in Eq. (18) and Eq. (19) and lead to ν=1 in Eq. (20). Under such approximations, Eq. (17) is transformed to

$$FV(\Delta)=\frac{\sqrt{C^2(\Delta)+S^2(\Delta)}}{P(\Delta)}=\frac{\left|\int_0^k I(k_z)e^{jk_z\Delta}dk_z\right|}{\int_0^k I(k_z)dk_z} \tag{28}$$

in which

$$C(\Delta)=2\int_0^k I(k_z)\cdot\cos\left((k_z-k)\cdot\Delta\right)dk_z \tag{29}$$

$$S(\Delta)=2\int_0^k I(k_z)\cdot\sin\left((k_z-k)\cdot\Delta\right)dk_z \tag{30}$$

$$P(\Delta)=2\int_0^k I(k_z)dk_z \tag{31}$$

The second equation in Eq. (28) can be demonstrated by inserting Eqs. (29)-(31) into the left hand side of the equation followed by some mathematical rearrangement. Inserting Eq. (27) into Eq. (28), and denoting θ_d=asin(NA) (NA is the numerical aperture of the MMF), the fringe visibility is analytically expressed as

$$FV(\Delta)=\frac{\left|\int_{k\cos\theta_d}^k e^{jk_z\Delta}dk_z\right|}{k(1-\cos\theta_d)}=\left|\text{sinc}\left(\frac{\phi}{2}\right)\right| \tag{32}$$

where $\phi=\frac{k\Delta(1-\cos\theta_d)}{2}$, Δ is the OPD of the FP cavity. Equation (32) is in complete agreement with Eq. (8) in Ref [14], the deduction of which is based on ray-optics. Equation (32) predicts that under 'uniform mode excitation' condition, the visibility curve is solely determined by the numerical aperture of the fiber. In Ref [15], the authors analyzed three types of fibers, whose parameters are listed in Table 1.

Table 1. MMF Parameters[a]

	Fiber		
Parameter	*1*	*2*	*3*
2*a* (μm)	100	50	50
n_1	1.448	1.448	1.448
n_2	1.440	1.416	1.440
NA	0.15	0.30	0.15
V number	30.80	30.68	15.40

[a] Numbers obtained from Appl. Opt. **43**,4659 (2004)

#151186 - $15.00 USD Received 15 Jul 2011; accepted 29 Aug 2011; published 8 Nov 2011

Fiber 1 and 3 have the same NA but fiber 1 has a much larger mode volume; fiber 1 and 2 have similar mode volumes, but the NA of fiber 2 is twice that of fiber 1. Computer simulation results based on the exact mode analysis [15] and based on Eq. (32) are compared in Fig. 8. It is clearly shown that the results from the two theories agree well, except little discrepancies due to inaccuracy of Eq. (32) induced by the approximations. The fringe visibility for Fiber 2 drops much faster than Fiber 1 and 3 cases due to its larger NA; in contrast, the visibility curve is not affected directly by mode volume. Although Fiber 1 has a much larger mode volume, its fringe visibility appears to be similar to that of Fiber 3; Fiber 2 shows much worse fringe visibility compared to fiber 1, yet they have similar mode volumes.

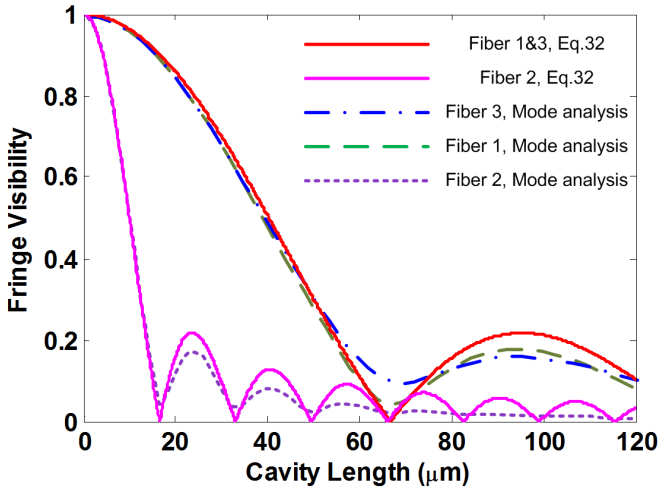

Fig. 8. Fringe visibility versus FP cavity length for fiber 1,2 and 3, all modes are equally excited. Simulation is based on Eq. (32) and the fiber mode analysis method in [15].

3.3 MMF-EFPI: simulation and experimental results

We use the system configuration shown in Fig. 4 for the measurement of the fringe visibility of MMF-EFPIs. A fiber coupled thermal light source (HL-2000 Tungsten Halogen Source, Ocean Optics, Inc.) with broadband incoherent radiation was used to illuminate a multimode fiber (MM-S105/125-22A, Nufern) with core diameter of 105μm and NA=0.22. We used a 50/50 MMF coupler (MMF:100 μm core, 0.29NA) to replace the circulator, the extra arm of the coupler was immersed in refractive index matching fluid for anti-reflection. The signal from the EFPI was recorded using an Optical Spectrum Analyzer (AQ6315A, Ando Electric Co., Ltd.) with spectral resolution set to 1 nm; the fringe visibilities at 800nm, 1200nm and 1550nm were measured.

#151186 - $15.00 USD Received 15 Jul 2011; accepted 29 Aug 2011; published 8 Nov 2011

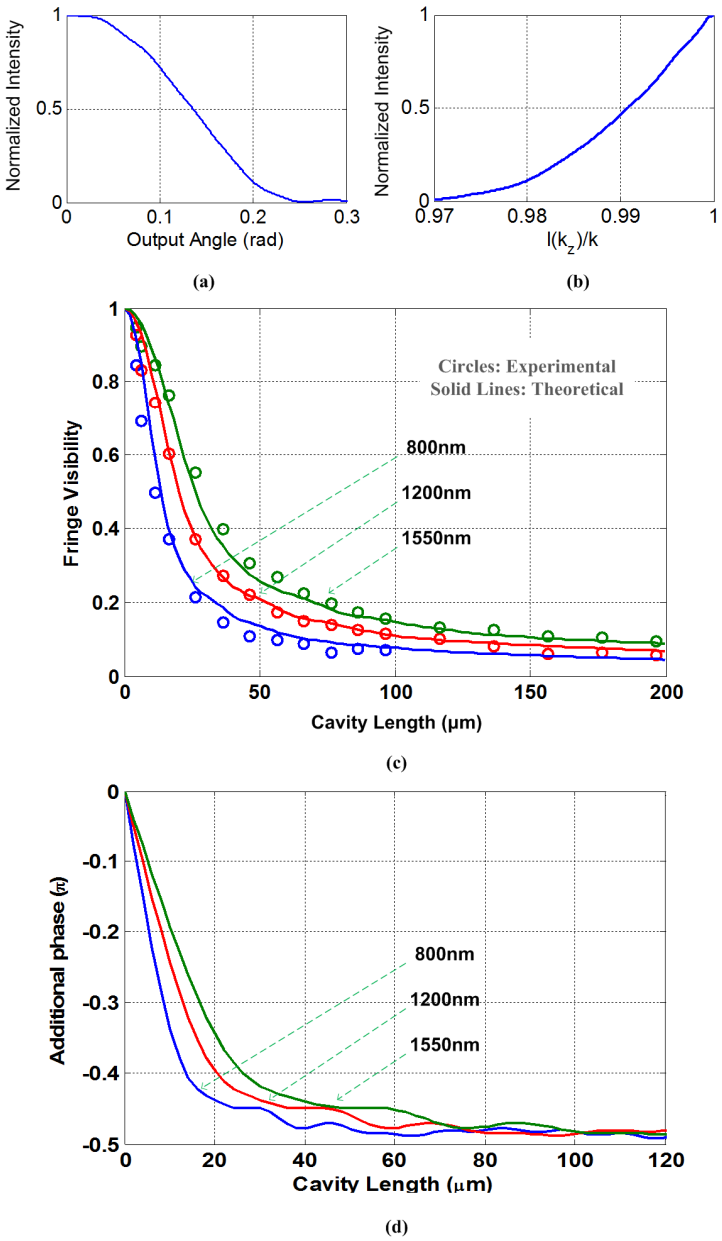

Fig. 9. Theoretical and experimental results of the fringe visibilities and additional phases versus OPD for MMF-EFPI. MMF has core diameter 105μm and NA=0.22. (a) Measured angular distribution. (b) Calculated $I(k_z)$ distribution based on (a). (c) Fringe visibility versus OPD curve for 800nm, 1200nm and 1550nm light, theoretical and experimental. (d) Additional phase θ versus OPD for 800nm, 1200nm and 1550nm light, theoretical.

Due to mode filtering and mixing, the uniform mode excitation condition discussed in Section 3.2 is rarely satisfied in reality; instead, the power distribution among the excited modes tends to stabilize during propagation, establishing an equilibrium mode distribution, and creating a far-field intensity distribution similar to a Gaussian. However, assuming the angular distribution as Gaussian and use Eq. (25) to calculate $I(k_z)$ leads to large errors in the calculated fringe visibility. In fact, the fringe visibility curve is very sensitive to the shape of

#151186 - $15.00 USD Received 15 Jul 2011; accepted 29 Aug 2011; published 8 Nov 2011

the angular intensity distribution; as a result, we used measured angular distribution to deduce $I(k_z)$, based on which the fringe visibility was calculated.

In order to measure the angular distribution, we measured the far-field intensity distribution using a beam profiler (BP104-IR, Thorlabs, Inc.), the linear intensity distribution was then mathematically converted to angular distribution by characterizing the distance between the fiber distal end and the profiler; the $I(k_z)$ distribution was then calculated using Eq. (25), fringe visibility was then calculated based on $I(k_z)$ and Eqs. (17)-(20). In Eq. (20), light coupling coefficient ν was calculated by [22]

$$\nu = a^2 \Big/ \left(a + \Delta \cdot \tan\theta_d\right)^2 \tag{33}$$

where a is the fiber core radius, and Δ and θ_d are defined in Eq. (32). The measured angular distribution, measured $I(k_z)$ distribution and the calculated/measured fringe visibility curves are plotted in Fig. 9(a)-(c) respectively. Figure 9(c) demonstrates a good agreement between the theory and experiment. The calculated additional phases (based on Eq. (16)) for the three wavelengths were plotted in Fig. 9 (d). Due to the insufficient SNR in the experiment, we were unable to provide reliable measurement results for the additional phase. From the results, it is interesting to note that both the fringe visibility and the additional phase are dependent on wavelength. This is a natural outcome due to the fact that $I(k_z)$ varies with wavelength. The same principle shown in Fig. 6 also applies here: longer wavelength corresponds to narrower $I(k_z)$ distribution, which implies broader fringe visibility curve.

3.4 Further discussion

The most distinctive and important conclusion of the theory developed in this paper is that the fringe visibility of a fiber optic EFPI is determined by the power density distribution projected onto the z axis ($I(k_z)$ distribution) and the working wavelength. Temporal and spatial coherences of the illumination light, however, do not affect the fringe visibility.

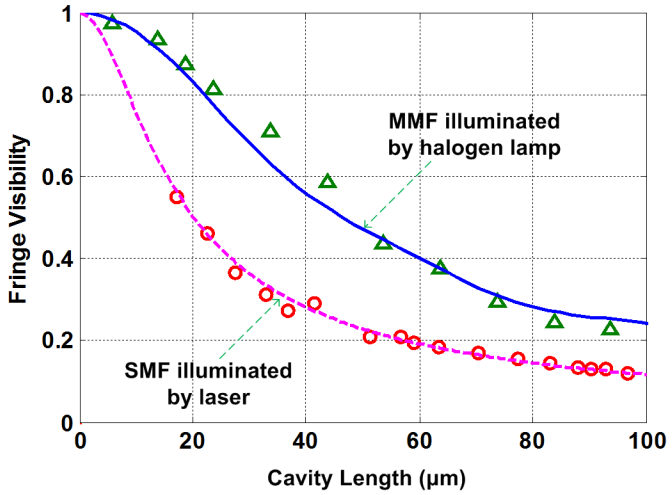

Fig. 10. Comparing the fringe visibility curves of two EFPIs. Due to its smaller output divergence angle, an MMF-EFPI illuminated by halogen lamp shows better fringe visibility than a SMF-EFPI illuminated by a highly-coherent laser.

Figure 10 shows the fringe visibility versus OPD curves for two types of EFPIs, both working at 1550nm. The first type is a single mode fiber based EFPI (SMF: UHNA7, Nufern), illuminated with a tunable laser whose coherent length is over 30cm (built-in fiber laser from the Component Testing System, Si-720, Micron Optics Inc.). The second is based on a multimode fiber (MM-S105/125-12A, Nufern) with core diameter of 105μm and NA =

#151186 - $15.00 USD Received 15 Jul 2011; accepted 29 Aug 2011; published 8 Nov 2011

0.12. The mode volume of the fiber is estimated as ~240 at 1550nm. The fiber was illuminated using a fiber-coupled halogen lamp (HL-2000 Tungsten Halogen Source, Ocean Optics, Inc.). The first EFPI configuration had perfect temporal and spatial coherences, while the second configuration was regarded as incoherent both temporally and spatially. However, due to the larger output divergence angle, the fringe visibility of the first EFPI was worse.

We also envision some potential applications and engineering impacts rest on the theory. The transform pair formed by the k_z distribution and the interferometer output enables us to characterize the output mode profile of an optical fiber by measuring the output intensity from a FP interferometer formed by the fiber endface and another partial reflection mirror. For example, for SMF, by fitting the visibility curve shown in Fig. 5, the mode field diameter of the fiber can be calculated at principally any wavelength above cutoff given the capability to measure the fringe visibility at that wavelength. For MMF, the visibility curve was observed to be very sensitive to the far-field intensity distribution of the fiber. Fitting the visibility curve thus provides an alternative means to characterize the output pattern of the fiber at any given wavelength.

The theory also implies some major considerations for optical fiber EFPI sensing system design. In order to have higher fringe visibility (higher SNR), the output divergence angle of the fiber needs to be decreased, either by reducing the NA or suppressing higher-order modes in the fiber; longer working wavelength also helps to increase the fringe visibility. For applications with critical SNR requirements, the near infrared range would be a better choice for sensing system design. For most EFPI sensor geometries, the OPD change within the full measurement range will not be large. The model also dictates that the additional phase shift will always stay within $[-\pi/2,0]$ for both MMF-EFPIs and SMF-EFPIs, which initiates the hope for complete elimination of the signal demodulation jumps [12].

4. Conclusion

A theoretical effort to model the interference spectra of low finesse fiber optic Fabry-Pérot interferometers is presented in the paper. The deduction of the theory was based on a rigorous diffraction treatment of the field in the FP cavity, and through some reasonable approximations, we reached a transform pair between the interferometer output and the spatial power density distribution projected onto the direction normal to the reflection mirrors. After some further approximations, it was found that the above relationship reduced to a Fourier-transform problem, which was analogous to the Fourier transform pair formed by the output intensity of a Michelson interferometer and the spectrum of the optical source used to illuminate the interferometer. The theory was experimentally proven using both single-mode fiber and multimode fiber based EFPIs, and we sought to establish relationships between the new model with previously published theoretical approaches. We found that the fringe visibility and additional phase in the interferogram were strongly influenced by the output spatial power density distribution and working wavelength, but were not directly related to either temporal or spatial degree of coherence. Some potential applications and optical fiber sensing system design guidelines were also discussed.

Acknowledgements

The authors would like to thank Liguo Kong of the Department of Chemistry, Virginia Tech, for the inspiring discussions. The work was supported by the National Energy Technology Laboratory (NETL) of the U.S. Department of Energy under grant DE-FC26-99FT40685.

#151186 - $15.00 USD Received 15 Jul 2011; accepted 29 Aug 2011; published 8 Nov 2011